Remote Sensing of Environment 261 (2021) 112469

Contents lists available at ScienceDirect

Remote Sensing of Environment

journal homepage: www.elsevier.com/locate/rse

Coastal morphology from space: A showcase of monitoring the topography-bathymetry continuum

Erwin W.J. Bergsma [a,b,*], Rafael Almar [c], Amandine Rolland [d], Renaud Binet [a], Katherine L. Brodie [e], A. Spicer Bak [e]

[a] Centre National d'Etudes Spatiales (CNES), 18 Av. Edouard Belin, 31400 Toulouse, France
[b] CNES-LEGOS (Laboratoire d'Etudes en Geophysique et Oceanographie Spatiales), UMR5566, 14 Av. Edouard Belin, 31400 Toulouse, France
[c] IRD-LEGOS (Research Institute Pour Le Developpement - Laboratoire d'Etudes en Geophysique et Oceanographie Spatiales), UMR5566, 14 Av. Edouard Belin, 31400 Toulouse, France
[d] THALES SERVICES, 290 allée du Lac, 31670 Labège, France
[e] U.S. Army Engineer Research and Development Center, Coastal and Hydraulics Laboratory, 1261 Duck Rd, Duck, NC, United States

ARTICLE INFO

Keywords:
Topography
Bathymetry
Coastal zone
VENμS
Spaceborne monitoring

ABSTRACT

With a large part of the world's population residing in coastal areas, and largely depending on the coastal environment, monitoring natural and human-induced coastal changes are paramount to understand the dynamic and vulnerability of these coastal systems/communities. To understand changes in coastal areas, e.g. environmental and social resilience to environmental change, local measurements are inadequate. Such large-scale issues can only be addressed with perhaps less accurate but large scale measurements from space. Considering vulnerability or exposure to coastal flooding, both the bathymetry (underwater) and topography (above water) are vital boundary conditions to understand and accurately estimate impacts on short (storms) and long (inter-seasonal) time-scales. In this work, we estimate the coastal bathymetry and topography with the optical VENμS satellite for every single overpass at the Field Research Facility of the US Army Corps of Engineers at Duck, NC. The experimental VENμS satellite enables estimation of the topography and bathymetry by two repetitive identical images with a small time-lag. This capability proofs to result in topographies with a few meters accuracy and the bathymetry estimation is at best a few decimetres accurate. As a base for future Earth Observation missions such as Landsat or Sentinel 2, VENμS shows that higher resolution imagery (5 m), repetitive bands and a revisit time of only 2 days, enables unprecedented land/sea monitoring.

1. Introduction

Most of the world's population resides within 50 km of seas or oceans. Measuring and gaining an understanding of coastal-zone dynamics over broad spatial and temporal scales are paramount to predicting and mitigating potential threats to these environments. As population densities increase in coastal regions, impacts of coastal erosion may be exacerbated by a desire to restrict natural variability and maintain present-day coastal morphology. Much of our understanding of coastal zone processes have been derived from local studies, and often with a focus on storm-dominated environments in first world countries. However, coastal zone issues are gaining visibility around the world, and as a result, demand for new techniques for collecting coastal morphology data are increasing. Traditional techniques using RTK-GPS and echo-sounding systems are often the most accurate and precise, but can also be time-consuming and expensive, particularly if broad regional surveys (over 100's of km) are required. Ultimately, several surveys are required to observe and gain an understanding of coastal-zone dynamics, natural and forced. Land-based or airborne remote sensing techniques, that reconstruct topographies (shoreline tracking or stereo-reconstruction) and bathymetries (through depth-inversion using wave kinematics), can cover the temporal component –delivering bathymetries near-constantly, and daily topographies– but still lack large (100's of km) spatial coverage. Satellite Earth Observation is an emerging observation technique with applications to coastal zone management because of the frequent temporal resolution and large spatial scales (global) (Benveniste et al., 2019).

Over the last decades, and accelerated over the most recent decade,

* Corresponding author at: Centre National d'Etudes Spatiales (CNES), 18 Av. Edouard Belin, 31400 Toulouse, France.
E-mail address: erwin.bergsma@cnes.fr (E.W.J. Bergsma).

https://doi.org/10.1016/j.rse.2021.112469
Received 8 December 2020; Received in revised form 18 April 2021; Accepted 21 April 2021
Available online 1 May 2021

global optical satellite imagery is systematically acquired on a regular basis with, for example, NASA's Landsat and EU Copernicus/ESA's Sentinel constellations with high resolution (10 to 10s of meters). All of this optical-imagery is also freely available to anyone, and through third-party platforms like Google' Earth Engine (Traganos et al., 2018) or Amazon' AWS, they are attainable in large quantities and at large scale –something that used to be reserved for Space Agencies. It is this particular combination that allows for larger scale, community-based analysis of coastal parameters worldwide (Bergsma and Almar, 2020). An example of engaging the research community to extract coastal observations relates to shoreline tracking (Vos et al., 2019; Luijendijk et al., 2018). While shoreline positions are an indicator of beach state and one can extract signs of erosion or accretion (or a trend of), it only reveals part of the picture. For full understanding of coastal evolution one should aim to measure beach-topography –by constructing a Digital Surface Model (DSM) (Almeida et al., 2019) – and nearshore bathymetry (among others Lyzenga (1978); Stumpf et al. (2003); Poupardin et al. (2016); Poursanidis et al. (2019); Caballero et al. (2019); Pike et al. (2019); Bergsma et al. (2019)). While bathymetries can be obtained by using those publicly available data, the topography can not due to the form of which the data are distributed – the minimum publicly-available data-level is Level 1C (Top of Atmosphere) while satellite-sensor level data is required (Level 1A). The DSM capability of optical satellites is largely reserved for those satellites that have the capability to view the same scene with different angles such as ALOS-PRISM (JAXA) –maximum 3 scenes– (Tadono et al., 2014) or an agile satellite, like Pleiades (CNES) –maximum 12 scenes.

In this work we aim to extract beach topography and bathymetry during a single overpass, using an exploratory Earth Observation satellite, VENμS, designed to serve as a laboratory for testing new techniques and methodologies. Like Landsat or Sentinel 2, VENμS systematically collects data but with a 2-day revisit interval and 5.3 m resolution. The unique capabilities of the VENμS satellite enable DSM and bathymetry reconstruction for every single overpass. We provide details on the satellite imagery in the following section, followed by a description of the study-site, bathymetry inversion algorithm, and DSM reconstruction methodology. In the Results, section bathymetry inversion and DEM reconstruction are presented and evaluated in comparison to in-situ measured data. The discussion focuses on the ability to capture morphological evolution and the potential for future Earth Observation missions.

2. Methods

2.1. Satellite mission and data collection

In this work, an experimental satellite mission for Earth Observation is used to obtain sub-aerial and sub-aqueous coastal elevation data which are analyzed through time to quantify coastal dynamics. The Vegetation and Environment monitoring on a New Micro-Satellite (VENμS) mission is a joint –ISA (Israeli Space Agency) and CNES (French Space Agency)– mission that aims to execute technical and scientific experiments that could form a basis for future optical missions. The technical, experimental part, consists of in-flight orbit transfer while the scientific experiments are focused on new image processing techniques. Around 100 specific sites are covered globally with a revisit of every 2 days. Data used in this article is acquired from a sun-synchronised Low-Earth-Orbit with 98.27° inclinations at 720 km altitude. The VENμS satellite has a super-spectral optical instrument onboard consisting of 12 Visible Near-InfraRed spectral bands that deliver imagery at a 5.3 m ground-resolution. The first and last spectral bands (respectively band 5 and 6) are identical with the purpose of Digital Surface Model (DSM) reconstruction. In addition to DSM reconstruction of the beach topography, we use these two bands in this work to estimate the nearshore bathymetry. Considering the high-revisit frequency of every two days, we aim to evaluate whether these data can be used to quantify coastal morphology evolution.

For this study VENμS is set to acquire image-data covering the US Army Engineer Research and Development Center's Field Research Facility in Duck, North Carolina, which is located at the east coast of the USA (illustrated in Fig. 1a-c). The FRF is a coastal observatory particularly known for the high quality, consistent data collection with a high spatio-temporal resolution of both, hydro- and morphodynamics for more than 4 decades (established in 1977). Hydrodynamic observations, including water levels (tides), waves, and currents are measured using in-situ gauges (e.g. waverider buoys, pressure gauges, and acoustic Doppler instruments) and more recently with remote sensing technology, including terrestrial LiDAR (Brodie et al., 2015; O'Dea et al., 2019). The morphology (topographies and bathymetries) is measured monthly using amphibious vehicles (either the Coastal Research Amphibious Buggy (CRAB) or Lighter Amphibious Resupply Cargo Vessel (LARC)) with mounted echo-sounding/GPS/motion detector systems (Forte et al., 2017), as well as hourly using terrestrial LiDAR (O'Dea et al., 2019) and video systems (Holman and Stanley, 2007). These continuous morphodynamic observations make the FRF an attractive place to test new technologies and methods. Data collected at the FRF have been shown valuable in the past for the validation of various bathymetry estimation techniques with shore-based or UAV-mounted video (Brodie et al., 2018; Brodie et al., 2019), high altitude (2.8 km) aerial photography (Dugan et al., 2001), video dwell length test (Piotrowski and Dugan, 2002; Holman et al., 2017), and colour based satellite-derived bathymetry (Lyzenga et al., 2006).

At the FRF, the tailored acquisition setup for VENμS covered a 55 km stretch along-track and a 27.56 km swath width (across-track), passing Duck in the northern side of the image such that enough land area is covered to properly geo-rectify the satellite imagery. The image-acquisition zone is indicated by the green outlined area in Fig. 1d. The large footprint of the satellite image highlights the regional potential of satellite coastal observations; that is the observation region is large in comparison to the typical survey domain – the white box in Fig. 1d – around the FRF – red dot in Fig. 1d. Here, the satellite-derived bathymetries will be compared to the in-situ LARC measurements. These LARC measurements are collected monthly which allows for testing if the satellite-derived bathymetries are accurate enough to observe nearshore morphology evolution through time. The topography is compared to airborne LiDAR (Wozencraft and Lillycrop, 2006) that covers similar coastal stretch as the VENμS imagery.

2.2. Satellite-derived bathymetry approaches

Linear wave theory has been used as early as the Second World War to derive beach slopes from areal photographs taken of enemy-held beaches (Williams, 1947). Yet, it was only in the early 2000s, with the digitisation of video cameras, that wave-kinematics were used systematically to measure beach morphology with reasonable accuracy from elevated shore-based camera systems (Stockdon and Holman, 2000). Developments over the last decades (Almar et al., 2008; Holman et al., 2013; Bergsma et al., 2016; Bergsma and Almar, 2018; Simarro et al., 2019) shows that bathymetries can be estimated with O(10 cm) accuracy in various wave-climates and tidal regimes using video cameras, but the infrastructural needs of such systems limit the spatial coverage to at best a few square kilometres. The bathymetry inversion algorithms developed to utilize these shore-based observation techniques exploited the fixed nature of the camera systems and the long-dwell videos that they collected (e.g. tens of minutes). In contrast, satellite-based imagery of the nearshore often lacks temporal dwell; that is, for non-geostationary satellites, given their velocity, a video of *at best* a minute or so can be obtained. For more (publicly) available satellite data, such as SPOT or Sentinel 2, approaches have recently been developed to extract wave propagation information and estimate bathymetry with an accuracy of O(m) between only 2 image snapshots with a small amount of time in between (Mancini et al., 2012; Abileah, 2013; Poupardin

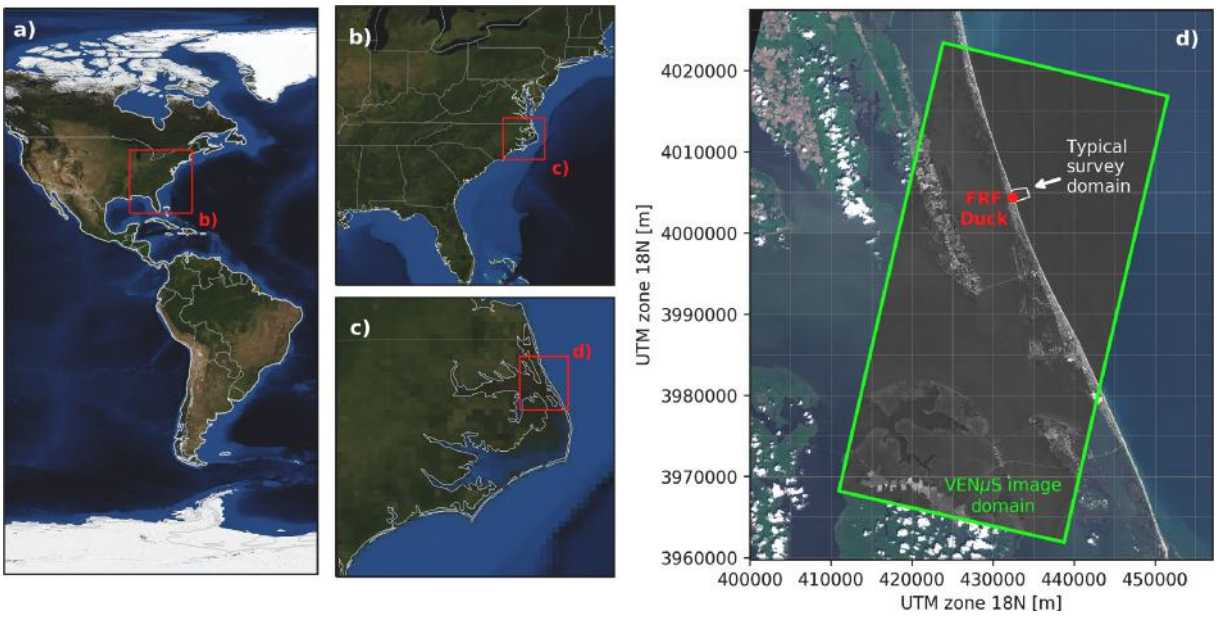

Fig. 1. Location overview for the study-site, the US Army Corps of Engineers, Field Research Facility (FRF), at Duck, North Carolina, USA. a-c provide the overview, zooming in to d). Where d) shows the area covered by VENμS outlined in green, the location of the USACE-FRF is represented by the red dot and the typical in-situ survey domain covered by the Lighter Amphibious Resupply Cargo (LARC) vehicle measuring campaigns is indicated by the white perimeter. (For interpretation of the references to colour in this figure legend, the reader is referred to the web version of this article.)

et al., 2016; Almar et al., 2019; Bergsma et al., 2019). In addition to these wave-kinematics based approaches, techniques to derive bathymetry from satellites using light reflectance through the water column have also been developed and have similar accuracy, O(m) (among others; Lyzenga (1978); Caballero et al. (2019); Caballero and Stumpf (2019)). Both approaches have great potential to enable worldwide coastal zone monitoring, particularly when considering the frequent revisit rate of Sentinel 2 (Bergsma and Almar, 2020). However, currently, the accuracy of the satellite-based techniques is one order larger than operational shore-based video cameras and two-orders larger than in-situ echo-soundings. Hence, additional research is needed to reduce these errors so that satellite techniques can be useful for coastal scientists, engineers and managers regularly.

2.2.1. *Bathymetry inversion algorithm updates*

The bathymetries in this work are derived following a similar approach outlined in (Bergsma et al., 2019), in which a local Fourier Slicing technique is used to estimate wave propagation. However, we deviate from Bergsma et al. (2019) after the Radon-sinogram Eq. (1) is constructed from a sub-sampled image around a point of interest where we want to know the depth:

$$R_I(\theta,\rho) = \iint_D I(x,y)\ \ \delta(\rho - x\ \ cos(\theta) - y\ \ sin(\theta)\ )\ \ dy\ \ dx \tag{1}$$

where $I(x,y)$ is the sub-sampled image, δ a Dirac-function, ρ the beam-length and θ the rotational angle. The size of the sub-sampled images is user-defined and here we use sub-sample domains of 600 × 600 m. The typical beam-length of the Radon Transform –ρ– is linked to the size of this sub window at $\theta = 0$ degrees –hence in this case 600 m. This beam is then rotated 360 degrees with a degree interval, resulting in the Radon-sinogram $R_I(\theta,\rho)$. In (Bergsma et al., 2019), a discrete Fast Fourier Transform (FFT) was applied to the Radon-sinogram to extract the wave parameters needed to solve the linear dispersion Eq. (8). An FFT in combination with varying windows sizes, however, leads to inconsistent results due to the dependency of the frequency-resolution (df) on the sub-window size and pixel-resolution. In addition, a constant frequency resolution (df) means that the spatial resolution is greater for smaller wavelengths and coarse –often too coarse– for the longer wave lengths to accurately resolve wave propagation. To overcome this, a direct Discrete Fourier Transform (DFT) is applied with a variable frequency resolution that is wavelength dependent (e.g. higher frequency-resolution is used for longer wavelengths). Of course, utilizing a DFT instead of an FFT slows down the computation (e.g. computational complexity: $O(n^2)$ vs $O(n\ \log\ (n))$), but considering the typical window sizes of a few hundred meters in x and y and dx, dy of 5 m at minimum, the effect on the computational time is limited, yet the gain in accuracy large. Following the notation in Birgham (1988) but adapted to the Radon Transform and applied over a given angle (θ), a discrete Fourier transform can be applied using:

$$\widetilde{H}(k) = \sum_{n=0}^{N-1} h_n(\rho) e^{-2\pi i k n/N} \tag{2}$$

wherein $\widetilde{H}(k)$ is the discrete Fourier approximation of a continuous Fourier transform, $h_n(\rho)$ is the input signal per given angle –here obtained from the Radon-sinogram over beam-length ρ–, k represents the angular wavenumber (frequency in space), n the current sample and N is the total number of samples. One can use the DFT (2) to apply it to a range of preset wave-numbers. Here we limit the angular wavenumbers associated with offshore wave periods (T) ranging from 3 to 25 s with a ΔT of 0.05 s.

Like any other spectrum, amplitudes and phases can be derived from the complex coefficients in the Radon-Fourier spectrum. At this point, we have a spectrum $\widetilde{H}(k,\theta)$ per time step (per detector band), for the user-defined range of frequencies –or angular wave numbers (k)– over all Radon-directions (θ). Here we want to select the waves' to use for the inversion carefully and we set three criteria: 1) most energetic spectral components, 2) only physically meaningful wave-phase shifts (we will elaborate what meaningful means below) and 3) select shorter waves in shallow water and longer waves in deep water. The first can be derived with the spectral amplitudes while the latter requires a bit more insight. Let's start by computing the spectral wave phase-shifts between two detector-bands that supply images at two different times (t and $t + 1$):

$$\Delta\Phi(k,\theta) = tan^{-1}\left(\frac{\Im\left(\widetilde{H}_{t+1}(k,\theta)\widetilde{H}_t\left(k,\theta\right)^*\right)}{\Re\left(\widetilde{H}_{t+1}(k,\theta)\widetilde{H}_t\left(k,\theta\right)^*\right)}\right) \quad (3)$$

in which $\widetilde{H}(k)$ represents the DFT (k,θ) per image (at time t and $t+1$), the superscript * denotes the complex conjugate while $\Im$ and $\Re$ respectively indicate the imaginary and real part of the cross product. To limit non-physical wave-number/direction selections, the spectrum is filtered using physical wave propagation limits so that only physically meaningful wave propagation are allowed. Considering that the time difference between two frames (here $\Delta t = 2.669$ s) is known, one can approximate the minimum and maximum wave-propagation limits per angular wave number over this Δt using linear wave theory ($c^2 = \frac{g}{k}tanh(kh)$). The minimal wave propagation relates to the shallow water reduction of the linear dispersion relation –tanh(kh) → 0 = kh– so that $c = \sqrt{gh}$. Now the minimal phase shift can be determined as a function of a given minimal depth:

$$\Delta\Phi_{min} = \Delta t k\sqrt{gh_{min}} \quad (4)$$

wherein k are all user-defined angular wave numbers, g is the gravitational acceleration (set to 9.8 m/s^2 here) and h_{min} is the minimum water depth. The minimal water depth depends on the image resolution where the starting point is that at least 2 pixels displacement (pixel size = Δxy) is required to observe wave propagation. Considering this, the minimum phase shift simplifies to:

$$\Delta\Phi_{min} = 2k\Delta xy \quad (5)$$

Similarly, a maximum phase shift ($\Delta\Phi_{max}$) can be determined based on the deep water limit, as $kh \to \infty$, tanh(kh) becomes 1 and thus $c = \frac{g}{2\pi}T$ and considering that $c = L/T$, the wave length L becomes $\frac{g}{2\pi}T^2$. Using this, one can limit the maximum phase shift in terms of the angular wave number (k) to:

$$\Delta\Phi_{max} = \frac{\Delta t}{\sqrt{\frac{1}{gk}}} \quad (6)$$

Spectral phase-shifts ($\Delta\Phi$) outside these set limits are considered non-physical and are set to zero. The amplitude and phase spectrum are then multiplied to extract energetic and propagating signals only, within our set boundaries. For N (default =3) resulting most energetic spectral energy peaks, the celerity is approximated using:

$$c = \frac{\Delta\Phi}{k\Delta t} \quad (7)$$

Then depth can be approximated using the sensed wave celerity c and associated angular wavenumber k to solve the linear dispersion relation for free surface waves:

$$h = \frac{1}{k}tanh^{-1}\left(\frac{c^2k}{g}\right) \quad (8)$$

Noteworthy, throughout Eqs. (1)–(8) only three user-defined inputs are required: 1) number of frequencies to analyse, 2) the minimum depth (default = 0.5 m) and 3) range of resolved wave periods (default = 3–25 s). The latter two inputs can be considered applicable to a large range of wave conditions all over the world and could be set to constants.

2.2.2. Wave selection and combining multiple waves

Besides that wave celerities are limited within a physical range, a preference for shorter over longer waves in shallow water and vice-versa for deepwater should also be considered. An elegant way of taking this into account is including additional restrictions based on $\gamma = \frac{c^2k}{g}$ (Stockdon and Holman, 2000; Simarro et al., 2019) – applied in a similar way using the wave period in Bergsma and Almar (2018). Restrictions based on γ have a similar origin and are linked to the $\Delta\Phi$ limits but instead of an a priori limit, the endogenously estimated c and k are used to compute γ. Similar to $\Delta\Phi$ limits, we can express the limits of γ as $\gamma \to 1$ means that particular wave is close to the deep-water limit, while when $\gamma \to 0$ will be the coastline. γ is smaller for longer waves in greater water depth; and the longer the wave, the more one can expect non-linearity and the less morphological details can be resolved. Bearing this in mind, we restrict allowable γ values based on the transitions from deep to intermediate and intermediate to shallow water to promote the selection of the appropriate waves at the transition zones while in intermediate water we don't mind. The deep water to intermediate water boundary is typically $h/L = 0.25$ (Komar, 1998) and the transition from intermediate to shallow water occurs around $h/L = 0.05$. These transition-values result in γ to be restricted to $0.3 < \gamma < 0.9$, as illustrated in Fig. 2.

The number of frequencies to analyse determines the number of estimated depths, if found, per point (x, y) of interest. All individual resulting depths passed the γ restriction, and to combine all individual depths they are weighted using γ. Direct weighting using γ entails that the closer the wave is to its deepwater limit (presumably more linear), the stronger it contributes to the weighted depth. The final result is a single map of depth to which several estimates contribute.

2.2.3. Study specific settings and tide

There are several user-defined parameters that must be determined for bathymetry estimation to work and for the bathymetry to be georeferenced. All bathymetries shown in this work are estimated over a domain around Duck, NC between $432000 < x < 435000$ and $4003500 < y < 4005500$ meters in UTM 18 N coordinates at a 50 m resolution. For the depth estimation method rest two more parameters, the maximum number of frequencies to analyse and the sub-sampling window size. Here we analyse at maximum 4 frequencies and set the sub-window to 600 × 600 m.

Once depths are derived the bathymetry has no vertical reference; it just represents the depth calculated at that instance. In order to compare the satellite derived bathymetries to in-situ measured data one needs to include the tidal elevation. At Duck the field measurements and the tidal gauge data are supplied with the same vertical reference (NAVD88), to get from depth to vertical referenced depth we just have to subtract the tidal elevation from the derived depths.

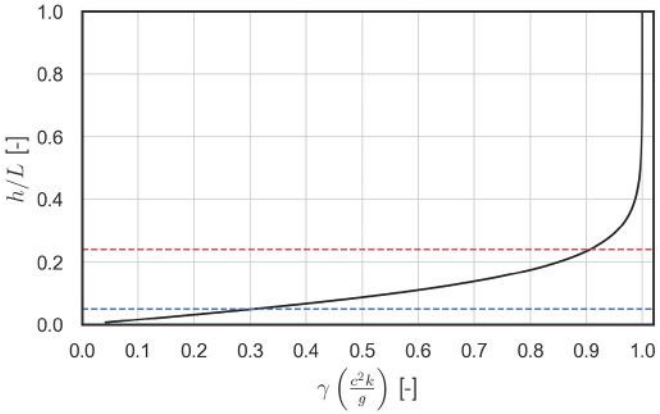

Fig. 2. Limits based on γ. The black curves represent h/L as a function of γ. The horizontal red dashed line indicates the transition from deep to intermediate water (0.25) while the blue dashed line represents the transition from intermediate to shallow water (0.05). (For interpretation of the references to colour in this figure legend, the reader is referred to the web version of this article.)

2.3. Topography from space

Besides a bathymetry, we aim to also obtain a topography to complete the coastal continuum at the same overpass of the VENμS satellite. To get a digital surface model, at least two frames covering the same location from different angles are required so that the stereoscopic principle can be applied. The VENμS satellite provides this possibility through two identical detector bands (same spectral content) at the start and end of the image acquisition; in other words, Band 5 and 6 are placed at the extremities of the focal plane. This process is illustrated in Fig. 3, where at time *t*, band 5 (blue rectangle) is acquired and 2.7 s later, band 6 (red rectangle) is acquired looking at the same position from a different angle.

A topography is obtained through spaceborne stereoscopy, which can be achieved by correlating observed local deformations to a local elevation. To do so it requires geometric information of the satellite, hence, at minimum Level 1A products are required; products that are radiometrically corrected and in sensor geometry (so not ortho-rectified such as Sentinel 2 Level 1C or higher levels). This product level is often restrictively available to public users, and similarly, for VENμS this information is only available through the Image Quality Center (VIQ) at the French Space Agency (CNES).

After the conversion from payload data (Level 0) to sensor level data (Level 1A), the first step is to perform a geometric correction using Geopix. For the geometric correction, image tie points are computed between detector bands 5, 6 and 7 of the L1A product. Ground control points are computed with respect to a Sentinel 2 reference image covering the same scene to correct the VENμS Level 1A product to an absolute location. Now we have a refined geometric model that drastically decreases correlation errors related to persistent attitude restitution uncertainties. After correcting the geometric model, a disparity map between band 5 and 6 is computed. This correlation, measured using QPEC/Medicis tool (Cournet et al., 2016), is performed without re-sampling B5 and B6 bands in a common geometry. Instead, to avoid noise from the re-sampling process, the co-location grid from band 5 to 6 images is computed from the corrected geometric model to give an a-priori on B5/B6 disparity. At this point, we get a disparity map at a reduced resolution every 4 pixels which is then used to compute the correlation between these disparities using a window 21 × 21 pixels (see the section below). Band 5 and 6 tie points are then derived from valid correlations. Now we have tie-points between the image from band 5 and 6, the viewing direction intersection is computed from these tie points – where the lines meet in Fig. 3 – which leads to a local elevation. The result is a Digital Surface Model with an intrinsic resolution of 50 × 50 m. The DSM is finally obtained in sensor geometry (B5 band geometry) and compared to a reference DTM to assess the altitude restitution performance (Rolland et al., 2019). An overview of the DSM global processing chain is presented in Fig. 4.

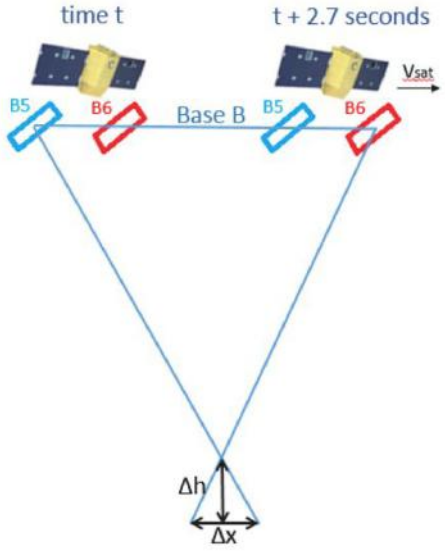

Fig. 3. Illustration of the stereoscopic capability provided by the VENμS satellite. By collecting two images that look at the same scene but at a different angle a Digital Surface Model can be calculated (Δh) through correlation of shifted (Δx) ground tie-points.

2.3.1. Correlation window

A stereoscopic system is characterised by its base to height ratio (B/H). Whereas regular B/H ratios are around 0.15 (e.g. the very high-resolution Pleiades satellite) or tailored 3D missions such as ALOS-PRISM with a B/H ratio of 1.0, VENμS has a small B/H ratio of 0.025. This B/H ratio is similar to the ratio found at SPOT5 between Panchromatic and Multispectral images (May and Latry, 2009). The main advantages of such small B/H ratio are a good radiometric similarity between images and no occlusion areas (interest in mountainous and urban areas). However, as the disparity between images is smaller, the resulting DEM is more sensitive to geometric modelling errors and has a less important altimetric sensibility. To overcome this drawback, we lower matching noise by increasing the size of the correlation window up to 21 × 21 pixels, which in turn may yield a fattening effect in the resultant Digital Elevation Model (DEM). One could choose a smaller window but this decreases the correlation stability and hence increases noise levels.

2.3.2. Geometric errors and their correction

Unfortunately, VENμS imagery is subject to attitude restitution errors which restrict accurate DEM retrieval. Despite a correction performed at VENμS ground segment (Binet et al., 2018), attitude residuals yield interband image misregistration of 0.2 pixels RMS; which is a significant value for most remote sensing applications. Due to the low B/H ratio of 0.025 between stereo bands B5 and B6, this misregistration induces an error of 40 m RMS. Therefore, a new attitude correction, based only on the image's content, is developed using the geometric toolbox (Geopix – developed at CNES) to achieve a registration accuracy of maximum 0.05-pixel (Bernardini et al., 2020). This method uses tie points computed between several bands. Note that a-priori knowledge of the tie points altitude (based on SRTM DTM) is required to constrain the attitude correction. As shown in Bernardini et al. (2020), the correction on the VENUS imagery collected at DUCK leads to very good interband-registration performance of maximum 0.05 pixel, ultimately reducing vertical offsets in the DSM.

3. Results

A total of 112 VENμS satellite images meet the cloud-coverage criterion (cloud coverage <40%) considering the whole image, over a period from 4 April 2019 to 26 August 2020. However, locally around the FRF clouds could still exist while passing the 40% criterion and sometimes wave patterns were not visible or orbital noise too pronounced. As a result, the number of estimated bathymetries over this period is limited to a total of 42. Nonetheless, on average we are able to obtain a bi-weekly satellite-derived bathymetry. For the coastal topographies derived by stereo-reconstruction, 6 dates were selected rather than all imagery due to the complexity of data accessibility (sensor-level) and processing chain.

3.1. Bathymetry

Within the set of 42 derived bathymetries, the skill and accuracy of the estimation method varies, depending on environmental conditions such as wave characteristics, atmospheric conditions such as clouds, and finally the degree of which wave propagation is observable (depending on image clarity, noise, etc). Later on, we will discuss a time series of

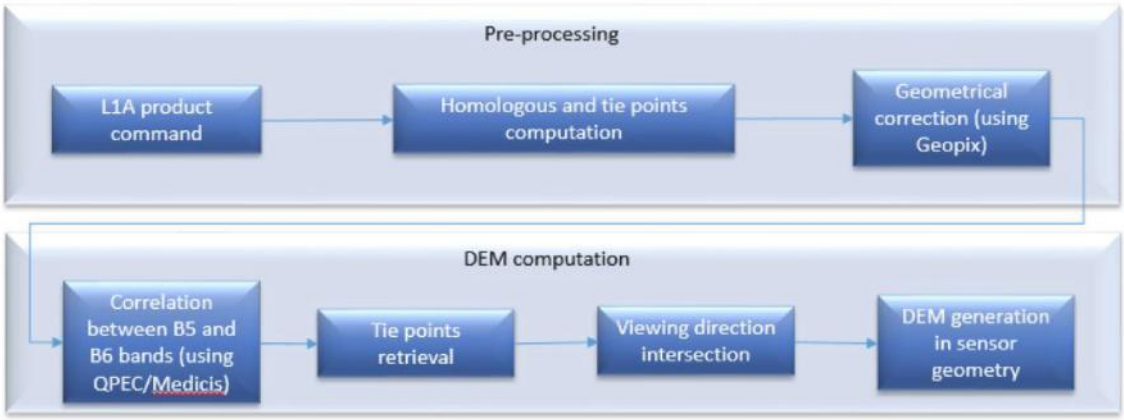

Fig. 4. Overview of VENμS DEM processing chain.

bathymetry but to illustrate the method's performance let us show an example of this wave-kinematics based bathymetry estimation at 50 m resolution over a 2 × 3 km domain around Duck.

While the depth is the final objective, intermediate parameters generally provide a good qualitative indicator of the performance one can expect to get. Ultimately one is after a proper wave direction and a wave celerity that are in the order from 0 and 15 m/s. The stream plot in Fig. 5 provides clear confidence in the estimated wave direction, wave refraction patterns are visible as waves arrive closer to shore. Also, the colouring indicating the wave celerity shows that the wave celerity reduces as the closer waves get to shore, as one would expect. This provides some confidence in both, the wavenumber and phase-shift estimation. Fig. 5c shows the derived water depths on 16 May 2020. It is important to note that not every cell in the domain meets the filtering limitations (see Methods section) or wave propagation is perturbed (e.g. due to white-capping, boats) and therefore at some parts of the domain

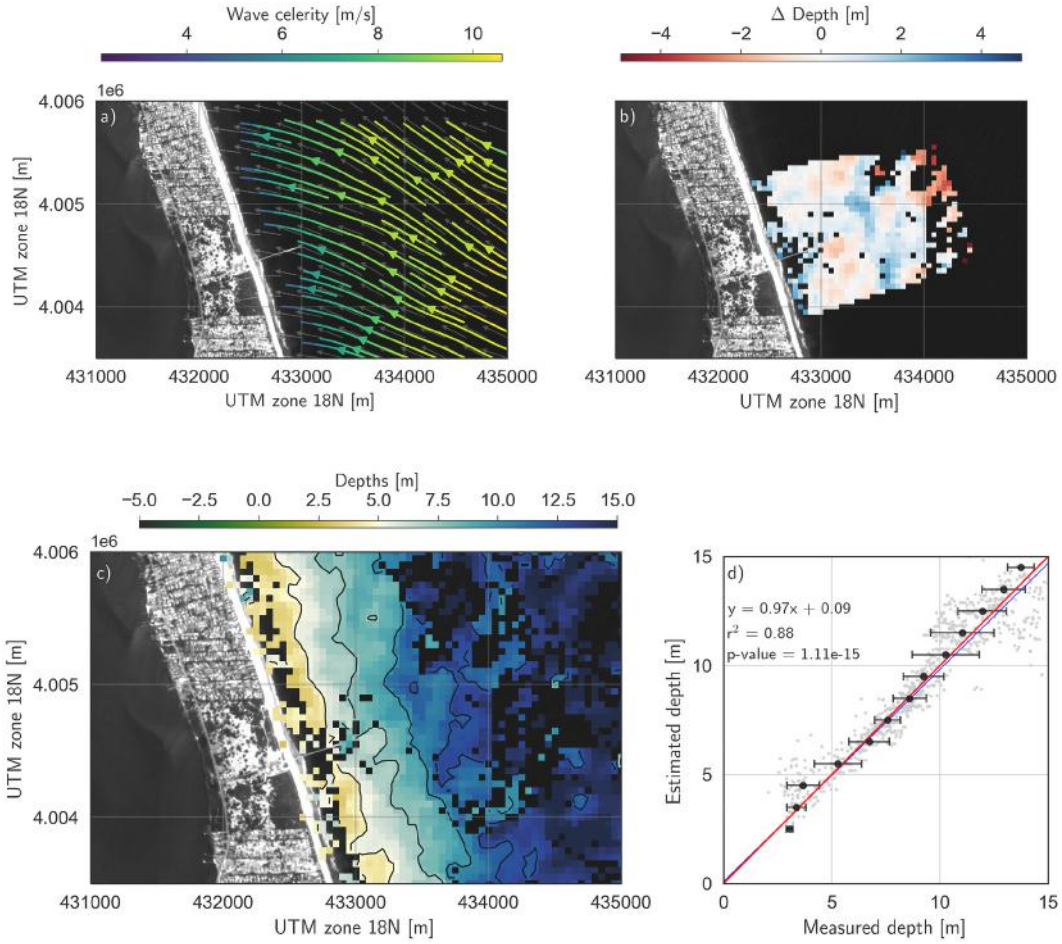

Fig. 5. A bathymetry estimation result using VENμS satellite imagery at the FRF DUCK, NC on 16 May 2020. From a) to d), a) represents the wave direction/celerity pattern, b) the difference between estimated and surveyed water depth, c) estimated water depth (NAVD88), d) scatter including basic statistics to illustrate the bathymetry estimation performance.

no depths could be derived. There are two regions where most non-returns are found: the shallowest and deepest parts of the domain. Although it is evident that the set limits primarily work in these regions, so one can expect no-returns, it is also true that these regions are more challenging with little time information (2 frames only). For example, the beach is a non-propagating bright (high pixel intensity) feature that hinders the estimation of wave propagation or leads to significant overestimation of the wavelength and is subsequently rejected by the γ-criterion (Section 2.2.2). In addition, the γ-criterion clearly rejects depth estimates in the offshore regions. Considering a measured wave period of 6.4 s and an offshore limit for depth estimation at $h/L = 0.25$ (Komar, 1998) one can expect to estimate depths until approximately 16 m. Although the accuracy and precision deteriorate towards deeper water, a similar depth estimation limit is found here.

Fig. 5b shows the difference of the derived bathymetry in comparison to a survey conducted with the LARC one day before the satellite pass-over (15 May 2020). Over the total domain represented in Fig. 5b we find an RMS error of 1.07 m and an average bias −0.04 m. Over the whole domain, the method is capable of estimating the depth within 4.1% of the measured water depth. If we consider an alongshore average cross-shore profile the RMS error is down to 84 cm while the average bias changes to 0.09 m. In addition to these statistical indicators, let's explore the sensing-error source(s) by using a measured bathymetry (that acts as known-depth) and a measured wave period so that an expected angular wave number and related celerity can be computed. This allows for assessing if the sensing-error is mainly made in k or c –thus $\Delta\Phi$–, or both over the entire inversion/survey domain. For wavenumber k an average bias of −0.0183 rad/m is found, this is a large relative error as it represents at worse an offset of 14.6%. The error can partially be contributed to the fact that angular wavenumber k is estimated over a sub-window using surrounding points –in comparison to instantaneous expected angular wavenumber k. Using a sub-window inherently leads to a smoothing of the rapidly changing wavenumber as the waves propagate to shore. The wave celerity is on average overestimated +0.44 m/s which is around 5.7% overestimation on average. Interestingly, an underestimated k and overestimated c partially compensate each other in γ; which is expressed in an average bias of 0.039 for γ. Similarly, a scatter plot as presented in Fig. 5d can provide us with valuable statistics as it represents the measured versus estimated depth. A perfect match is found when the grey and black dots lay on top of the diagonal red-line (1:1 line). It is evident from the scatter that there is a skill in the methodology to estimate water depths from satellite imagery with just 2 frames. The statistics confirm this with a linear fitting line with 0.97 slope and 0.09 intersect. The estimation captures a large degree of the variance – r^2 of 0.88 – which is significant – p-value < 0.05.

3.2. Topography

Satellite-based topographies can be derived for each acquired image but as mentioned earlier, due to computationally expensive routines and limited (secured) data access to the sensor-level data, we limit our focus in this section to 6 topographies at different dates. Previous work with very-high-resolution satellite data from Pleiades, shows that a topography through stereogrammetry can be accurate enough to monitor morphological change on the beach (Almeida et al., 2019). The performance of stereogrammetry is largely susceptible to what degree texture can be observed. Let's say that between Almeida et al. (2019) and this work, other than that there is much more water in the image at Duck, the environment is similar but one major difference can be found in how both satellites acquire their optical imagery. Let alone sensor differences, we find that the ground resolution of VENμS is about ten times larger than Pleiades which inherently means fewer details/texture could be observed, and hence fewer homologue tie-points to correlate with one another. At the same time, Pleiades is a relatively agile satellite that takes, by default two or three different images at relatively large incident angles (B/H ratios – in Almeida et al. (2019) the two images had a B/H ratio of 0.36) while VENμS is downward-looking, taking a single image (with different bands) through a push-broom image-acquisition concept which results in much smaller incident angles and weaker B/H ratio (0.025). While we hence do not expect a similar order of precision as in Almeida et al. (2019), VENμS imagery should be able to deliver topographies with reasonable accuracy, and considering VENμS' revisit time of 2 days (something that would be very expensive to do with Pleiades), precision and accuracy can be improved by assimilating topographies.

Fig. 6 is exemplary for the typical result one obtains by applying a stereogrammetry procedure to detector-band 5 and 6 of VENμS. Fig. 6 shows airborne LiDAR data and VENμS derived topography. A fundamental difference between these DEMs is that they are respectively a Digital Terrain Model and a Digital Surface Model, in which the LiDAR represents the bare terrain while VENμS topographies represent the top of a surface. Nonetheless, the LiDAR data is the most accurate available large-scale dataset to compare the VENμS derived topography against. From Fig. 6a one can see that the airborne LiDAR provides an elevation measurement along the whole open coast within the VENμS scene; the VENμS topographies are computed over the entire scene –Fig. 6b. There are 6 GPS-measured points (red-dots in Fig. 6b) that are open areas and can be used to co-locate all satellite-derived DEMs to the same vertical reference frame (Almeida et al., 2019) but also to assess its performance. The non co-located DEMs have an average RMS error of 4.99 m and a bias of 0.09 m. in comparison to an airborne LiDAR survey, an RMS error of 7.83 m is found and a bias of 0.48 m. This error seems enormous but it should be placed in context. In comparison to well known DEMs – such as NASA's SRTM (radar) and JAXA' ALOS-PRISM (optical), with a respective vertical accuracy of 6–9 m (Farr et al., 2007), 7 m (Tadono et al., 2014)– that are composites of several over-passes, a similar accuracy is found for VENμS (Rolland et al., 2019). Unlike the specialised optical missions ALOS-PRISM and Pleiades, VENμS has the least favourable angle and resolution configuration. The pixel' ground resolution (10 times less than Pleiades) and small B/H ratio (40 times smaller than ALOS-PRISM / 6 times smaller than Pleiades) are the weakest for VENμS between the three missions leave improving the accuracy difficult: to get to this accuracy, boundaries are pushed to get up to 0.05 pixel accurate position determination. Considering, any unforeseen satellite movement, even the tiny vibrations, will contribute to a similar order of errors. If we zoom in to an area of 3 × 3 km around the FRF (Fig. 6c-e) and compare Fig. 6c and e visually, we see that in general, large morphological dune features are present and in the right order of magnitude.

3.3. Coastal continuum

Ultimately the satellite-derived bathymetry and topography combined enables the monitoring of full coastal evolution, including beach morphodynamics and dune development –and their interlinked morphological behaviour (de Vries et al., 2012; Ruessink et al., 2018). Here we present an alongshore average continuum profile to show the potential of acquiring satellite-derived topography and bathymetry in a single over-pass of the VENμS satellite. The satellite-derived results are compared to the airborne LiDAR which is presented in Fig. 7a. The alongshore average profile of the LiDAR data (black) and VENμS derived profile (red) are presented in Fig. 7b.

From the first look at Fig. 7b it is evident that the satellite-based alongshore average profiles of both the topography and the bathymetry show great potential. Although, around the shoreline and nearshore, in shallow water depths, the satellite data struggles to derive an elevation – likewise traditional echo-sounding / GPS based measurements that do not use an amphibious craft also suffer from this data-gap –, the bathymetry and topography estimation using VENμS has skill. The RMS error of the alongshore average topography and bathymetry are respectively 1.12 m and 0.84 m with a respective bias of +0.11 m and −0.10 m. As for the topography, this could be linked to accounting for

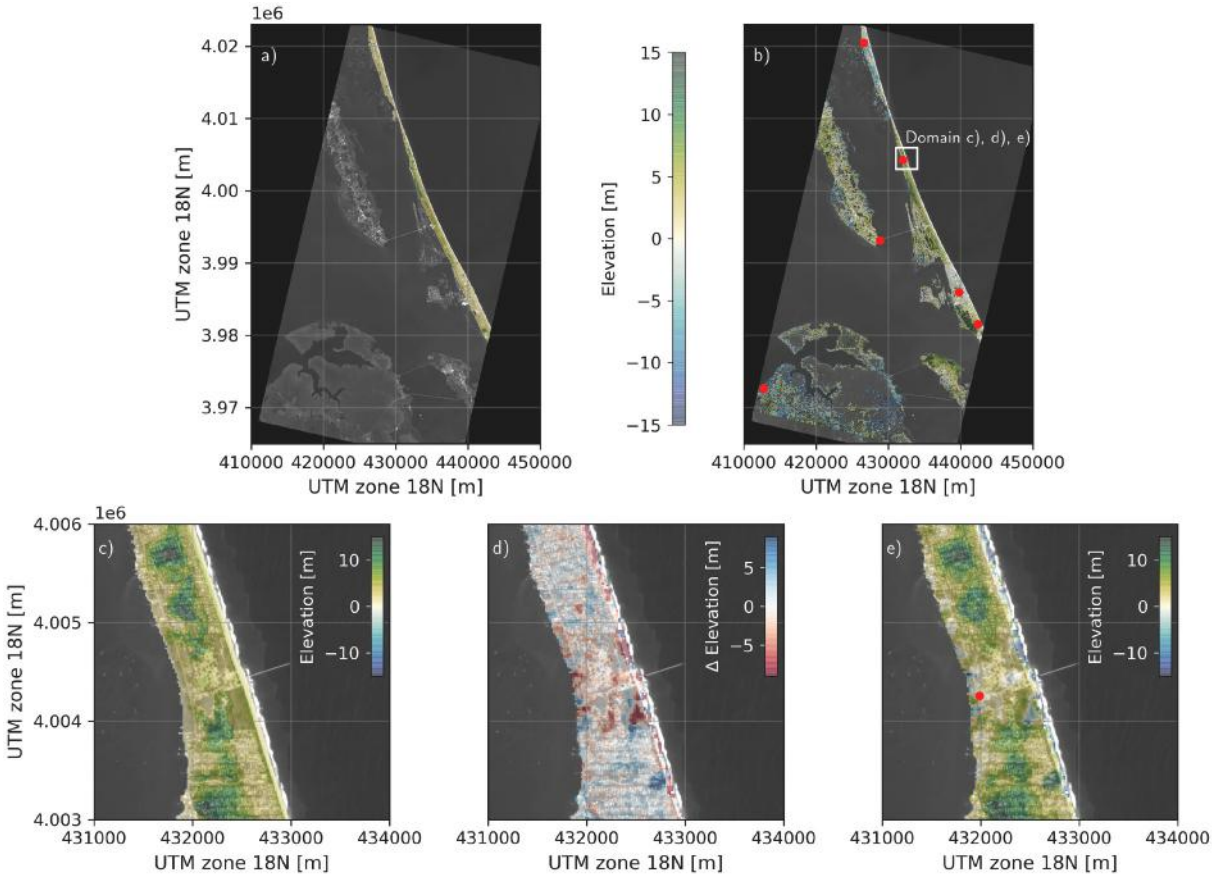

Fig. 6. Measured and satellite derived topographies. a) and b) show the DEMs over the whole VENμS acquisition scene (30 × 50 km) of respectively airborne LiDAR DTM (18 to 25 June 2019) and VENμS imagery based DSM (26 August 2020). c) to e) show a zoomed area (3 × 3 km) around the FRF, with respecively the airborne LiDAR in c), a difference plot between LiDAR and VENμS in d) and the VENμS DEM zoom in e).

vegetation or bare earth only. For the assessment of and protective measures against coastal inundation knowledge about the coastal maximum is important. The LiDAR finds an alongshore average coastal maximum –here the dune top– of 7.8 m while the VENμS satellite topography slightly underestimates the alongshore average coastal maximum with 7.2 m, a 60 cm (7%) vertical offset to the ground truth.

4. Discussion

4.1. Morphological evolution

Considering the results, monitoring coastal evolution –topography and bathymetry– at large spatial scales seems to be within reach. However, the results are presented at a single time while the performance likely varies in time. To address this, let us use alongshore average cross-shore profiles, plotted in time, and access whether coastal evolution monitoring is possible. Fig. 8 provides the basis for the analysis, including a temporal median profile in Fig. 8a, time-varying alongshore average cross-shore profiles presented as a time-stack in Fig. 8b and the associated error in comparison to the closest field survey (in time) carried out by the EDRC's LARC vehicle in Fig. 8c. The RMS-error is mainly associated with the bathymetry estimation since the topography is only estimated a few times over the same period.

Similarly to the results in Figs. 5 and 7, the performance of the bathymetry estimation is limited to the deepwater limit of the moment of sensing. Hence, in Fig. 8b the empty white areas on deeper sides. The red line in Fig. 8a, shows that the temporal average is very consistent (minimal standard deviation), until 12 m water depth. In deeper water, the method generally underestimates the water depth; which is most likely due to the weaker link between incident waves and the bathymetry. The greyed area –the standard-deviation in time– in Fig. 8a shows that the deeper limits follow the bathymetry deeper that 12 m, but are rarer in time. If the look at the time-stack in Fig. 8b, it is evident that there are some unnatural variations in the cross-shore direction but in general the method is capable of getting the cross-shore profiles right. At the shore, the satellite-derived bathymetries reveal a sandbar, which is unlikely to be this pronounced, nor present. From the temporal component in Fig. 8b and c it is clear that from Christmas 2019 until mid-February 2020 bathymetry estimations are rare; while during summer months bathymetry estimations are denser in time. This is mainly due to increased cloud cover during the winter months, so even with a two day revisit it is a challenge to obtain bathymetries regularly during these months. In the perspective of worldwide bathymetry estimation, this is a major limitation for tropical regions (Bergsma and Almar, 2020).

Fig. 8c shows the RMS error per VENμS bathymetry estimation compared against the closest LARC survey in time. The blue and orange bars indicate the RMS error related to the total profile (blue), and profiles until minimal offshore depth limit based on the wave period in time in orange (12 m). On average the bathymetries are estimated with an RMS error of 1.77 m, the best case shows an RMS error of 0.82 m and the worst has 2.95 m error over the full cross-shore profile. Focusing on the profiles until 12 m water depth (orange bars), the average RMS error reduces to 1.21 m and the worst stays similarly at 3.02 m while the best estimation goes down to 0.37 m. Although these results are promising and getting to a similar accuracy as video-based methods (Holman et al., 2013), it also holds that it would be a challenge to assess morphological change in the same order or smaller. The question that remains is if we

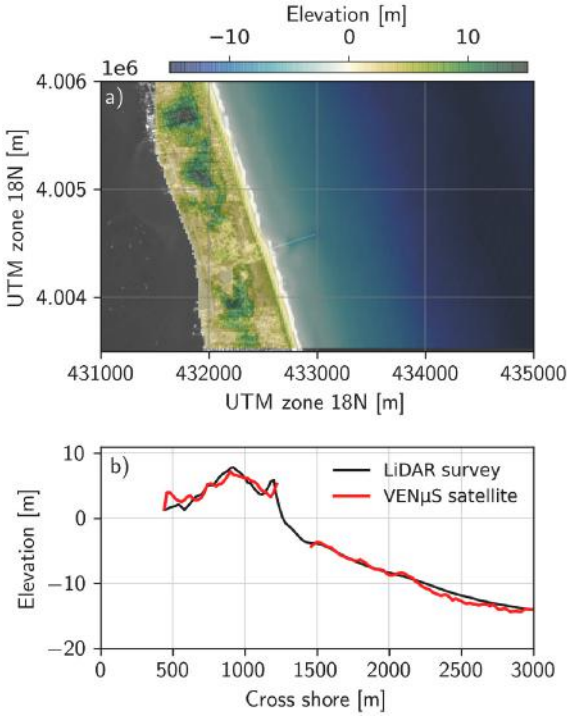

Fig. 7. Spaceborne coastal continuum. a) presents the airborne LiDAR measurements covering land and sea in the vicinity of the FRF at Duck overlayed on top of a Venus image. b) shows the alongshore average profile of the LiDAR survey in black and superimposed the VENμS derived topography and bathymetry in red. (For interpretation of the references to colour in this figure legend, the reader is referred to the web version of this article.)

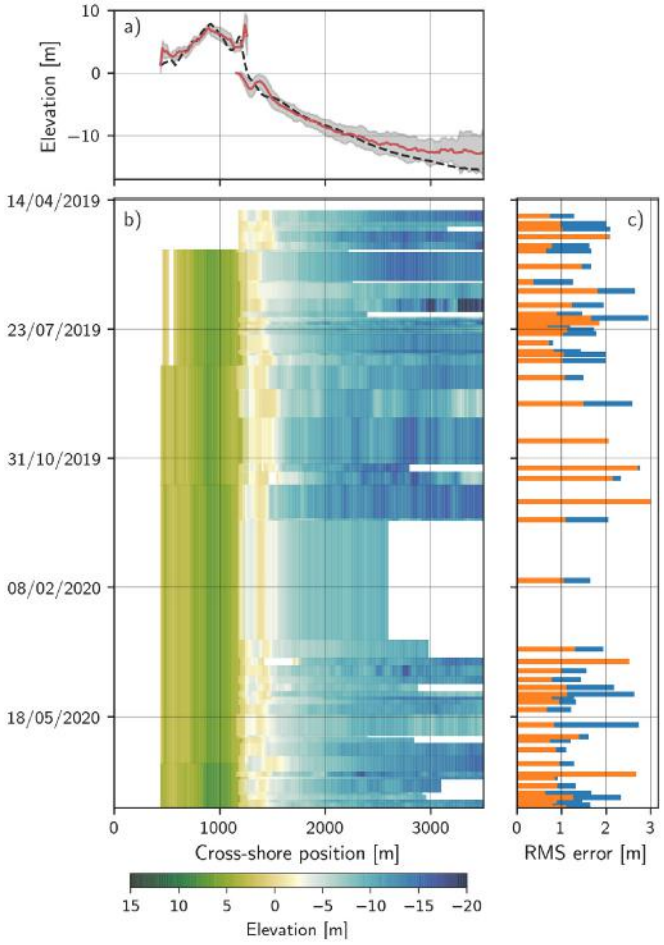

Fig. 8. Temporal evolution of alongshore continuum profiles showing in a) the temporal mean in red, with the standard deviation in time around the mean in grey. b) shows the time-stack of topography and bathymetry combined 18 April 2019 to 26 August 2020. c) represents the RMS error compared to the closest survey in time (maximum 1 month apart). The blue bars represent the error related to the full cross-shore profile, while the orange bars represent the RMS error until 12 m measured water depth (minimum offshore limit in time). (For interpretation of the references to colour in this figure legend, the reader is referred to the web version of this article.)

can link the accuracy to environmental conditions. Only weak to poor correlations are found compared to measured wave conditions; 0.21 correlation with the mean wave period and 0.06 correlation with the significant wave height. Although weakly correlated, we find that the shorter the waves the better the VENμS bathymetry-estimation.

4.2. *VENμS in perspective of the current Sentinel 2 mission*

The current Sentinel 2 mission shares many features with the VENμS satellite although the lower resolution (at best 10 m (Sentinel 2) instead of 5 m (VENμS)), the lack of repetitive, identical, detector bands (band 5 and 6 in VENμS) limits DSM construction for topographies and wave-propagation detection for nearshore bathymetries.

As for now DSM reconstruction using Sentinel 2 imagery is limited to overlapping ground-swaths using different orbits (Bergsma and Almar, 2020). The ground resolution of VENμS is a major limitation to further improve DSM reconstruction, with the current Sentinel 2 ground resolution of 10 m, DSM reconstruction is even more susceptible to small data-perturbations. More importantly, constructing coastal topographies from Sentinel 2 has another major limitation; data availability. Currently, the purest Sentinel 2 data (closest to sensor-level data) that is publicly available is restricted to Top of Atmosphere, Level 1C, while sensor-level data, Level 1A, is required. Hence, unless this user-policy is changed or DSM data is made available on a regular basis, DSM reconstruction with Sentinel 2 is not available to the broader public and remains a privilege for the European Space Agency (ESA) or space agencies alike.

Bathymetry estimation using light penetration physics e.g. (Lyzenga, 1978; Stumpf et al., 2003; Caballero and Stumpf, 2019) and wave kinematics can be done with the current levels of Sentinel 2 data (Bergsma et al., 2019). Focusing on the latter; considering that one is tracing wave propagation waves with a typical wave length in the order of 100 s meters, the satellite resolution –of 5 m (VENμS) and 10 m (Sentinel 2)– is sufficient to observe waves, but with a better resolution the wave propagation is potentially observed more accurately. As waves propagate into shallower water they become less and less dispersive: the phase speed of the wave is reducing towards shore resulting in wave shoaling; shorter wavelength greater water height hence steeper waves. Considering this, the observable wave pattern should be more distinctive (due to steeper waves) and one would expect a more accurate wavelength/propagation observation, and hence, the ability to estimate shallower water depths with higher resolution imagery. One major difference between VENμS and Sentinel 2, is the sensor configuration. While VENμS is a single detector with multiple bands, Sentinel 2 has multiple staggered detectors to enable a large, 290 km, ground-swath but these detectors collect data in opposite direction. This inter-detector variability has an effect on measuring propagating features (Yurovskaya et al., 2019) but also alters inter-detector intensities (hence products based on colour), especially on the boundaries of detector bands (Pahlevan et al., 2017; Medina-Lopez and Ureña-Fuentes, 2019).

4.3. An outlook to future systematic optical EO missions

Over the last decades, NASA's Landsat has been revolutionary by bringing satellite imagery to the public, and EU Copernicus/ESA's Sentinel programme is a solid supplement to systematic optical Earth Observation missions. The satellite used in this work is largely exploratory and there is no doubt that the VENμS mission is a tailored mission, and therefore quite flexible to user-demands to experiment acquisition modes for future applications. In many ways the VENμS satellite mission can be seen as a test platform for future Earth Observation constellation requirements (Landsat/Sentinel 2/other), and for this particular application to mount a case for next-level (topography and bathymetry) long-term, worldwide and standardised/repetitive coastal monitoring from space.

The main limitation of spaceborne coastal monitoring depends if one considers the emerged topography or the submerged bathymetry. For the topography, the weak B/H ratio of nadir satellites like Landsat and Sentinel 2, in combination with the ground resolution, is rather limiting the vertical accuracy. Considering that the B/H ratio is inherently bound to the space-craft configuration, one should opt for higher resolution; for example, closer to 1–2.5 m (similar to SPOT). Higher resolution will come at a price, needing to add more satellites or accepting a longer time in between revisits. For bathymetry estimation through wave kinematics, the resolution can be considered less important than for the topography but is required to solve fine morphological features. In general, for the bathymetry, if you have a very high-resolution satellite (resolution O(m) or sub meter), it does not mean you can observe the bathymetry more accurately. At some point, the finer resolution imagery does not improve the wave-physics estimation anymore but actual wave physics and their inherent lack in response to the bottom limit the bathymetry estimation. To illustrate this, a car (short wave) passing speed bump, feels the speed bump to a different degree than a lorry (long wave) passing the same speed bump in which a small bump is hardly felt by a lorry. In other words, a long period wave of 25 s is differently affected by complex morphology than a windsea wave of 5 s, and hence, with a wave of 5 s one can theoretically resolve finer morphological details. At the same time one has to bear in mind that the signal-to-noise ratio reduces. It is also not to say that image resolution is no limitation at all, in fact it is a significant limitation. Bergsma et al. (2019) shows that the Radon-Transform based Fourier Slicing method requires at least six points on a wave length, and with Sentinel 2. For Sentinel 2 bands at 10 m resolution this means that one can only resolve waves up to approximately 7 s. Future Sentinel constellation therefore do benefit from an increased resolution to for example 5 m, the method should then be able to resolve waves with 4.5 s periods. In addition to the resolution, one could consider the acquired imagery in terms of the number of frames. In this work 2 identical frames are used Bergsma et al. (2019) uses 2 frames from different colour-bands) but as one can imagine the more successive frames the more stable wavelength and celerity can be derived, or a better sense of the estimations' error could be obtained.

5. Conclusion

Using the *V*ENμS satellite we have obtained a first spaceborne remotely-sensed coastal continuum between land (topography) and ocean (bathymetry) with a single overpass. The topography and bathymetry are constructed using the same two frames with a small time difference. Novel methodological advances are presented, for example, the evolved bathymetry estimation routine. The topography is accurate to an order of a few meters, while for the bathymetry we find at best an RMS error of 0.37 m for depths shallower than the offshore deepwater limit while over a 1.5 year period the average RMS error is 1.21 m. The 2-day revisit enables bathymetry estimations at an unprecedented temporal density but these depend largely on the seasons: the most bathymetries are derived during the spring/summer months. This work shows the potential to obtain first-degree information on topography and bathymetry simultaneously using a generic Earth Observation setup similar to Landsat and Sentinel 2. Depending on the policy of data-availability, in particular sensor level data, the continuum capabilities to monitor our coastal environment as shown in this work remain restricted or could be unlocked to the larger public, new research and governing bodies.

Declaration of Competing Interest

The authors declare that they have no known competing financial interests or personal relationships that could have appeared to influence the work reported in this paper.

Acknowledgement

E.B. was funded through a post-doctoral fellowship of the French National Space Agency (Centre National d'Etudes Spatiales - CNES). We would like to thank the team in CESBIO, Toulouse –Gerard Dedieu and Olivier Hagolle– for enabling the image collection at Duck. We are indebted to everyone involved in the measurements, funding and programme at the US Army Corps of Engineers Field Research Facility at Duck, in particular Nicolas Spore, for data collection tailored to this project.

References

Abileah, R., 2013. Mapping near shore bathymetry using wave kinematics in a time series of worldview-2 satellite images. In: 2013 IEEE International Geoscience and Remote Sensing Symposium - IGARSS, pp. 2274–2277.

Almar, R., Bonneton, P., Senechal, N., Roelvink, D., 2008. Wave celerity from video imaging: a new method. In: Proceedings of the 31st International Conference Coastal Engineering, pp. 1–14.

Almar, R., Bergsma, E.W.J., Maisongrande, P., de Almeida, L.P.M., 2019. Wave-derived coastal bathymetry from satellite video imagery: a showcase with pleiades persistent mode. Remote Sens. Environ. 231, 111263.

Almeida, L.P., Almar, R., Bergsma, E.W.J., Berthier, E., Baptista, P., Garel, E., Dada, O.A., Alves, B., 2019. Deriving high spatial-resolution coastal topography from sub-meter satellite stereo imagery. Remote Sens. 11 (5).

Benveniste, J., Cazenave, A., Vignudelli, S., Fenoglio-Marc, L., Shah, R., Almar, R., Andersen, O., Birol, F., Bonnefond, P., Bouffard, J., Calafat, F., Cardellach, E., Cipollini, P., Le Cozannet, G., Dufau, C., Fernandes, M.J., Frappart, F., Garrison, J., Gommenginger, C., Han, G., Høyer, J.L., Kourafalou, V., Leuliette, E., Li, Z., Loisel, H., Madsen, K.S., Marcos, M., Melet, A., Meyssignac, B., Pascual, A., Passaro, M., Ribó, S., Scharroo, R., Song, Y.T., Speich, S., Wilkin, J., Woodworth, P., Wöppelmann, G., 2019. Requirements for a coastal hazards observing system. Front. Mar. Sci. 6, 348.

Bergsma, E.W.J., Almar, R., 2018. Video-based depth inversion techniques, a method comparison with synthetic cases. Coast. Eng. 138, 199–209.

Bergsma, E.W.J., Almar, R., 2020. Coastal coverage of esa' sentinel 2 mission. Adv. Space Res. 65 (11), 2636–2644.

Bergsma, E.W.J., Conley, D.C., Davidson, M.A., O'Hare, T.J., 2016. Video-based nearshore bathymetry estimation in macro-tidal environments. Mar. Geol. 374, 31–41.

Bergsma, E.W.J., Almar, R., Maisongrande, P., 2019. Radon-augmented sentinel-2 satellite imagery to derive wave-patterns and regional bathymetry. Remote Sens. 11 (16).

Bernardini, N., Binet, R., Vidal, B., Aug. 2020. Attitude restitution for multispectral earth observation satellite using space triangulation technique. ISPRS Ann. Photogramm. Remote Sens. Spatial Inform. Sci. 5 (1), 141–149.

Binet, R., de Lussy, F., Languille, F., Rolland, A., Gamet, P., Raynaud, J.-L., Specht, B., 2018. Venμs geometric image quality commissioning. In: Neeck, S.P., Martimort, P., Kimura, T. (Eds.), Sensors, Systems, and Next-Generation Satellites XXII, vol. 10785. International Society for Optics and Photonics, SPIE, pp. 66–78.

Birgham, E.O., 1988. The Fast Fourier Transform and Its Applications. Prentice Hall, Englewood Cliffs, New Jersey, 07632.

Brodie, K.L., Raubenheimer, B., Elgar, S., Slocum, R.K., McNinch, J.E., 2015. Lidar and pressure measurements of inner-surfzone waves and setup. J. Atmos. Ocean. Technol. 32 (10), 1945–1959.

Brodie, K.L., Palmsten, M.L., Hesser, T.J., Dickhudt, P.J., Raubenheimer, B., Ladner, H., Elgar, S., 2018. Evaluation of video-based linear depth inversion performance and applications using altimeters and hydrographic surveys in a wide range of environmental conditions. Coast. Eng. 136, 147–160.

Brodie, K.L., Bruder, B.L., Slocum, R.K., Spore, N.J., 2019. Simultaneous mapping of coastal topography and bathymetry from a lightweight multicamera uas. IEEE Trans. Geosci. Remote Sens. 57 (9), 6844–6864.

Caballero, I., Stumpf, R.P., 2019. Retrieval of nearshore bathymetry from sentinel-2a and 2b satellites in South Florida coastal waters. Estuar. Coast. Shelf Sci. 226, 106277.

Caballero, I., Stumpf, R.P., Meredith, A., 2019. Preliminary assessment of turbidity and chlorophyll impact on bathymetry derived from sentinel-2a and sentinel-3a satellites in South Florida. Remote Sens. 11 (6).
Cournet, M., Giros, A., Dumas, L., Delvit, J., Greslou, D., Languille, F., Blanchet, G., May, S., Michel, J., 2016, 06 2d Sub-Pixel Disparity Measurement Using qpec / Medicis. ISPRS - International Archives of the Photogrammetry, Remote Sensing and Spatial Information Sciences XLI-B1, pp. 291–298.
de Vries, S., Southgate, H., Kanning, W., Ranasinghe, R., 2012. Dune behavior and aeolian transport on decadal timescales. Coast. Eng. 67, 41–53.
Dugan, J.P., Piotrowski, C.C., Williams, J.Z., 2001. Water depth and surface current retrievals from airborne optical measurements of surface gravity wave dispersion. J. Geophys. Res. Oceans 106 (C8), 16903–16915.
Farr, T.G., Rosen, P.A., Caro, E., Crippen, R., Duren, R., Hensley, S., Kobrick, M., Paller, M., Rodriguez, E., Roth, L., Seal, D., Shaffer, S., Shimada, J., Umland, J., Werner, M., Oskin, M., Burbank, D., Alsdorf, D., 2007. The shuttle radar topography mission. Rev. Geophys. 45 (2).
Forte, M.F., Birkemeier, W.A., Mitchell, J.R., 2017. Nearshore Survey System Evaluation. Tech. Rep., ERDC-CHL Vicksburg United States.
Holman, R.A., Stanley, J., 2007. The history and technical capabilities of argus. Coast. Eng. 54 (6–7), 477–491.
Holman, R.A., Plant, N., Holland, T., 2013. Cbathy: a robust algorithm for estimating nearshore bathymetry. J. Geophys. Res. Oceans 118, 2595–2609.
Holman, R.A., Brodie, K.L., Spore, N.J., 2017. Surf zone characterization using a small quadcopter: technical issues and procedures. IEEE Trans. Geosci. Remote Sens. 55 (4), 2017–2027.
Komar, P., 1998. Beach Processes and Sedimentation, 2nd edition. Prentice-Hall.
Luijendijk, A., Hagenaars, G., Ranasinghe, R., Baart, F., Donchyts, G., Aarninkhof, S., 2018. The state of the world's beaches. In: Nature, Scientific Reports 8 Article 6641.
Lyzenga, D.R., 1978. Passive remote sensing techniques for mapping water depth and bottom features. Appl. Opt. 17 (3), 379–383.
Lyzenga, D.R., Malinas, N.P., Tanis, F.J., 2006. Multispectral bathymetry using a simple physically based algorithm. IEEE Trans. Geosci. Remote Sens. 44 (8), 2251–2259.
Mancini, S., Olsen, R.C., Abileah, R., Lee, K.R., 2012. Automating nearshore bathymetry extraction from wave motion in satellite optical imagery. In: Shen, S.S., Lewis, P.E. (Eds.), Algorithms and Technologies for Multispectral, Hyperspectral, and Ultraspectral Imagery XVIII, vol. 8390. International Society for Optics and Photonics, SPIE, pp. 206–217.
May, S., Latry, C., 2009, 01 Digital Elevation Model Computation with Spot 5 Panchromatic and Multispectral Images Using Low Stereoscopic Angle and Geometric Model Refinement, pp. 442–445.
Medina-Lopez, E., Ureña-Fuentes, L., 2019. High-resolution sea surface temperature and salinity in coastal areas worldwide from raw satellite data. Remote Sens. 11 (19).
O'Dea, A., Brodie, K.L., Hartzell, P., 2019. Continuous coastal monitoring with an automated terrestrial lidar scanner. J. Marine Sci. Eng. 7 (2), 37.
Pahlevan, N., Sarkar, S., Franz, B., Balasubramanian, S., He, J., 2017. Sentinel-2 multispectral instrument (msi) data processing for aquatic science applications: demonstrations and validations. Remote Sens. Environ. 201, 47–56.
Pike, S., Traganos, D., Poursanidis, D., Williams, J., Medcalf, K., Reinartz, P., Chrysoulakis, N., 2019. Leveraging commercial high-resolution multispectral satellite and multibeam sonar data to estimate bathymetry: the case study of the caribbean sea. Remote Sens. 11 (15).
Piotrowski, C.C., Dugan, J.P., 2002. Accuracy of bathymetry and current retrievals from airborne optical time-series imaging of shoaling waves. IEEE Trans. Geosci. Remote Sens. 40 (12), 2606–2618.
Poupardin, A., Idier, D., de Michele, M., Raucoules, D., 2016. Water depth inversion from a single spot-5 dataset. IEEE Trans. Geosci. Remote Sens. 119 (4), 2329–2342.
Poursanidis, D., Traganos, D., Chrysoulakis, N., Reinartz, P., 2019. Cubesats allow high spatiotemporal estimates of satellite-derived bathymetry. Remote Sens. 11 (11).
Rolland, A., Binet, R., Dick, A., Raynaud, J.-L., Mongin, L., Dedieu, G., Déjus, M., Nov. 2019. DEM Generation from Native Stereo Venμs Acquisitions.
Ruessink, B., Arens, S., Kuipers, M., Donker, J., 2018. Coastal dune dynamics in response to excavated foredune notches. In: Aeolian Research 31, 3–17, the Ninth International Conference on Aeolian Research - ICAR IX (Coastal Dune Processes and Aeolian Transport).
Simarro, G., Calvete, D., Luque, P., Orfila, A., Ribas, F., 2019. Ubathy: a new approach for bathymetric inversion from video imagery. Remote Sens. 11 (23).
Stockdon, H.F., Holman, R.A., 2000. Estimation of wave phase speed and nearshore bathymetry from video imagery. J. Geophys. Res. 105, 22015–22033.
Stumpf, R.P., Holderied, K., Sinclair, M., 2003. Determination of water depth with high-resolution satellite imagery over variable bottom types. Limnol. Oceanogr. 48 (1part2), 547–556.
Tadono, T., Ishida, H., Oda, F., Naito, S., Minakawa, K., Iwamoto, H., Apr. 2014. Precise global DEM generation by ALOS PRISM. In: ISPRS Annals of Photogrammetry, Remote Sensing and Spatial Information Sciences II4, pp. 71–76.
Traganos, D., Poursanidis, D., Aggarwal, B., Chrysoulakis, N., Reinartz, P., 2018. Estimating satellite-derived bathymetry (sdb) with the google earth engine and sentinel-2. Remote Sens. 10 (6).
Vos, K., Harley, M.D., Splinter, K.D., Simmons, J.A., Turner, I.L., 2019. Sub-annual to multi-decadal shoreline variability from publicly available satellite imagery. Coast. Eng. 150, 160–174.
Williams, W.W., 1947. The determination of gradients on enemy-held beaches. Geogr. J. 109 (1/3), 76–90.
Wozencraft, J.M., Lillycrop, W.J., 2006. Jalbtcx Coastal Mapping for the Usace (The International hydrographic review).
Yurovskaya, M., Kudryavtsev, V., Chapron, B., Collard, F., 2019. Ocean surface current retrieval from space: the sentinel-2 multispectral capabilities. Remote Sens. Environ. 234, 111468.